scientific reports

Check for updates

OPEN

Extraction, LC-QTOF-MS profiling of bacterial menaquinone (MK) and characterization of $CuFe_2O_4$ nanoparticles loaded MK: potential anti-cancer via gene expression

Reem M. Farsi[1]✉ & Mohamed S. Abdelwahab[2]✉

Ferrite nanoparticles (FNPs), especially copper ferrite nanoparticles ($CuFe_2O_4$ NPs), are a promising platform in nanomedicine for targeted cancer treatment. Consequently, unique $CuFe_2O_4$ NPs were functionalized with a bioactive extract derived from *Salinicoccus* sp. RM1, a halophilic bacterial strain obtained from the Red Sea. The bacterial extract, abundant in menaquinone (MK) homologs (MK-4 to MK-13) as verified by LC-QTOF-MS, used as an excellent functionalizing agent to produced MK-loaded nanoparticles ($CuFe_2O_4$ NPs-MK). Prepared NPs were analyzed using XRD, FT-IR, SEM, EDX, particle size analysis and magnetic susceptibility analysis, confirming the effective production and functionalization of the NPs. $CuFe_2O_4$ NPs modified with MK exhibited significant cytotoxicity against MCF-7 cells, yielding an IC_{50} of 48.94 µg/ml and a notable 45% reduction in *BCL-2* expression, while *BAX* expression experienced a marginal 3.4% rise. This study demonstrates its strength in innovative design and comprehensive characterization of a novel anti-cancer nanocomposite ($CuFe_2O_4$ NPs-MK), utilizing sustainably sourced marine MKs to induce apoptosis in breast cancer cells by modulating the BAX/BCL-2 gene ratio.

Keywords LC-QTOF-MS, Menaquinone (MK), $CuFe_2O_4$ NPs, Anticancer, Gene expression, MCF-7, BCL-2, BAX

Ferrite nanoparticles (FNPs) have become an essential material in the nanotechnology-driven revolution in biomedical research due to their distinctive superparamagnetic properties, biocompatibility, and adaptable surface chemistry[1,2]. These nanoparticles, primarily composed of iron oxides such as magnetite (Fe_3O_4) or maghemite (γ-Fe_2O_3), and frequently doped with transition metals like cobalt, manganese, or copper, enable precise magnetic manipulation for targeted drug administration, imaging, and hyperthermia-based cancer treatment[3].

Various techniques exist for synthesizing $CuFe_2O_4$ NPs, each influencing the physicochemical properties of the resultant material[2]. The predominant method is coprecipitation, entailing the concurrent precipitation of Cu^{2+} and Fe^{2+}/Fe^{3+} salts in alkaline conditions[4,5]. Metal alkoxide precursors are utilized in sol-gel techniques to produce homogeneous gels, which are subsequently calcined to generate crystalline nanoparticles[6–9]. Microwave-assisted techniques provide rapid, energy-efficient crystallization, whereas hydrothermal synthesis uses high-temperature, pressurized reactors to produce highly pure, monodisperse crystals[10–15].

Various techniques have been developed to alter the surface of ferrite nanoparticles, enhancing their functionality[16,17]. Polymer coatings, such as PEG and chitosan, enhance colloidal stability and biocompatibility. Silica shell encapsulation enables further functionalization with ligands or pharmaceuticals[18–20]. Biological functionalization, utilizing enzymes, antibodies, or bacterial extracts, imparts bioactive specificity, whereas inorganic metal coatings, such as gold, augment optical characteristics[21]. Bacterial extracts are an appealing option due to their intrinsic biocompatibility and versatile biochemical composition[22]. These extracts, serve as organic coronas that enhance the cytotoxicity and targeting capabilities of cancer cells[23].

[1]Faculty of Science, Department of Biological Sciences, King Abdul-Aziz University, Jeddah, Saudi Arabia. [2]Faculty of Education, Physics and Chemistry Department, Matrouh University, Mersa Matrouh, Egypt. ✉email: rfarsi@kau.edu.sa; mohamed-said-science@hotmail.com

Due to their adaptation to extreme environments, marine microbes generate distinctive secondary metabolites with significant characteristics. Biomolecules were effectively extracted using organic solvents. Through meticulous analysis of the extract using liquid chromatography-quadrupole time-of-flight mass spectrometry (LC-QTOF), bioactive substances were precisely identified [24[23,24],.

MK-1 to MK-13 are variants of vitamin K_2 synthesized by bacteria, possessing biological functions that extend beyond bone metabolism. The longer-chain variants (MK-7 to MK-10) have superior bioavailability and stability, resulting in prolonged effects on the body. Their capacity to regulate calcium-dependent proteins and redox processes renders them interesting in cancer therapy, as MKs may affect cell proliferation, induce apoptosis, and inhibit tumor growth by modulating oxidative stress and mitochondrial pathways[23,24].

The capacity of nanomaterials to modulate gene expression signifies a revolutionary advancement in precision medicine. Magnetic ferrite NPs excel in surface modifications that enhance endosomal escape and nuclear localization, while their super paramagnetism facilitates targeted delivery to specific tissues. The use of bioactive bacterial extracts enhances these methods by augmenting biocompatibility and precision in targeting[22,25–31]. With its complex etiology and wide range of clinical presentations, breast cancer continues to be a significant problem in the field of global health, making it difficult to treat and prevent[32]. There is growing evidence that a complicated combination of genetic, environmental, and lifestyle variables interacts to cause breast cancer carcinogenesis[33]. B-cell Lymphoma 2 (*BCL-2*) protein plays an anti-apoptotic role, preventing cell death. *BCL-2* is often overexpressed in cancer cells. *BCL-2* group members include *BAK* and *BAX*, which are pro-apoptotic elements that cause the release of cytochrome c, suppress mitochondrial function, and initiate apoptosis[34]. Actually, *BCL-2* and *BAX* have contrary activities[35]. It has recently come to light that *BCL-2* is a significant clinical prognostic indicator for breast cancer; approximately 85% of breast cancer tumors display higher protein levels of BCL-2[36].

This study demonstrates its strength in innovative design and comprehensive characterization of a novel nanocomposite ($CuFe_2O_4$ NPs-MK), utilizing sustainably sourced marine MKs to induce apoptosis in breast cancer cells by modulating the BAX/BCL-2 gene ratio. LC-QTOF was employed for a comprehensive investigation of the chemical constituents of the extract MKs. The altered NPs were meticulously characterized by X-ray diffraction (XRD) for crystallographic assessment, energy-dispersive X-ray spectroscopy (EDX) for elemental analysis, particle size analysis, and scanning electron microscopy (SEM) for morphological evaluation.

Materials and methods

Materials

Copper nitrate, Ferric chloride, Sodium hydroxide, HCl, Methanol, Ethanol, n-hexane, NaCl, Nutrient broth.

Methods

Seawater sampling and isolation of bacterial strain

Seawater samples were collected from the Red Sea near Rabigh City, Saudi Arabia. About 500 ml of seawater from different areas is collected in several sterile screw bottles and kept in the refrigerator till the isolation step. For each sample, before being transferred to agar plates for 72 h, one milliliter was mixed into sterile seawater nutrient broth (100 ml, pH 7 ± 0.2). The mixture was then incubated at 30 °C for 24 h while being shaken at 120 rpm. Following incubation, the colorful colony was selected, cleaned, subcultured, and preserved as a stock culture for future research[37].

Morphological and molecular identification

The morphological and Gram stain analyses of the marine orange bacterial strain were conducted after isolation and purification. Molecular identification of isolated bacteria was achieved by sequencing the 16S rDNA gene using the universal primer 785 F (5' GGATTAGATACCCTGGTA 3') and the reverse primer 907R (5' CCGTCAATTCMTTTRAGTTT 3') to amplify the 16 S rDNA region through polymerase chain reaction (PCR)[38], followed by sequencing[39], which, from similarity, can be investigated using the BLAST program[40]. A phylogeny tree was constructed using MEGA version 11.0.10[41,42].

Salinicoccus sp. RM1 growth conditions

Salinicoccus sp. RM1 growth (inoculum = 1%) was monitored under agitated conditions (120 rpm) in response to changes in temperature (20–40 °C), pH (5–10), and NaCl (0–15% w/v). The optical density measured at 600 nm over 48 h was used as a quantitative indicator[43].

MK solvent extraction

Salinicoccus sp. RM1 cells were harvested via centrifugation at 5,500 rpm for 5 min to separate the bacterial cells from the culture media. The separated cells were resuspended in methanol and stirred vigorously (500–700 rpm) for 2 h to facilitate the extraction of metabolites. The resulting methanolic extract was transferred to a separation funnel, and liquid-liquid extraction was performed using n-hexane (30 ml, three successive washes) to isolate non-polar impurities. The methanolic phase, containing the target analyte, was recovered. This fraction was subsequently dried at 35 °C and subjected to further analysis[23].

Preparation of $CuFe_2O_4$ NPs

0.1 M $FeCl_3$ and 0.05 M $Cu(NO_3)_2$ were synthesized in 100 ml of distilled water and agitated until fully soluble at 60 °C. 0.2 M NaOH was added dropwise to the solution, immediately forming a dark brown suspension. This solution is stirred for 2 h at 60 °C. The resultant solid was isolated, thoroughly rinsed with deionized water multiple times, dried, calcinated at 650 °C for 2 h, then ground into a fine powder and stored[44].

Preparation of $CuFe_2O_4$ NPs loaded with MK ($CuFe_2O_4$ NPs-MK)

Prepared $CuFe_2O_4$ NPs were mixed with MK at a 1:1 (w/v) ratio, kept at 30 °C until completely dry, and then stored in a dry place[45].

Characterization of the MK and NPs

Chromatographic conditions of LC-ESI-QTOF-MS

Chromatographic separation was performed using liquid chromatography coupled with mass spectrometry (LC-MS), operated in both positive and negative electrospray ionization modes (ESI+/-). The separation employed a binary mobile phase consisting of solvent A (water with 0.1% formic acid) and solvent B (acetonitrile with 0.1% formic acid), delivered at a constant flow rate of 0.500 mL/min under a high-pressure limit of 15,000 psi. A 20.00-minute linear gradient was applied, initiating at 95% A/5% B, transitioning to 100% B by 18.00 min (using curve type 6), holding for 1 min, and returning to initial conditions (95% A/5% B) by 20.00 min. Column temperature control was not enabled, and the gradient commenced at injection with automated seal washes every 5.00 min. Mass spectrometric detection utilized Time-of-Flight Mass Spectrometry with mass spectrometry enhancement (TOF-MS) capability, scanning a mass range of 100–1200 m/z. Data were acquired under two collision energy conditions: a low-energy function at 6 V and a high-energy function ramped from 15 V to 45 V[46].

Anti-breast cancer effect on *BAX* and *BCL-2* gene expression in MCF-7 cells

Cell culture

RPMI-1640 was employed for the development of human breast cancer cells (MCF-7). Streptomycin (100 mg/ml), penicillin (100 U/ml), and 15% FBS (Gibco Life Technologies, Grand Island, NY) were given to the medium as supplements. The cells were housed in a humidified atmosphere at 37 °C with 15% CO_2. Logarithmically growing cells were employed in all investigations[47].

Cytotoxicity of $CuFe_2O_4$ NPs-MK

For the purpose of investigating $CuFe_2O_4$ NPs-MK effects on the proliferation of MCF-7 cells, an MTT experiment was carried out. In 96-well plates, 2×10^4 cells/well were cultured. After 24 h, concentrations ranging from 3.9 to 1000 µg/ml of $CuFe_2O_4$ NPs-MK were introduced for a 48-h effect determination. Control wells, including cells without $CuFe_2O_4$ NPs-MK treatment and cells treated with $CuFe_2O_4$ NPs-MK, were treated with an equivalent amount (1%) of ethanol. Immediately after the treatment, the media was discarded, and MTT (200 µl of 2 mg/ml in PBS) was supplied to each well and incubated at 37 °C for 4 hours (5% CO_2). Thereafter, the contents of each well were removed, and 200 µl of DMSO was mixed by pipette and left for 45 s. Finally, the optical density (OD) was read with a multi-well microplate reader (ELIZA reader, Organon Teknika)[37].

Real-time PCR assay

An RT-PCR test was conducted to examine the expression of *BAX* and *BCL-2* genes following $CuFe_2O_4$ NPs-MK administration[48]. After 48 h of administration, cells were collected for RNA extraction (TransZol Up Plus RNA Kit, Cat. No. ER501, Transgenbiotech, China) and complementary DNA (cDNA) generation using the GScript First-Strand Synthesis Kit (Cat. MB305-0050, GeneDireX, Taiwan) as per the manufacturer's specifications. The A260/A280 ratio is applied to evaluate RNA quality using a NanoDrop microvolume spectrophotometer. cDNA synthesis was conducted according to the protocol, employing 2 µg of pure RNA as the template. The real-time PCR mixture consisted of SYBR Green qPCR Master Mix 2x (Cat. No. AQ601, TransGen Biotech, China) (10 µl), a mixture of both reverse and forward primers (2 µl), cDNA (2 µl), and H_2O (6 µl). The amplification condition was established as follows:

preincubation	15 min at 95 °C
Denaturation	45 cycles for 10 s at 95 °C
Annealing	30 s at 58 °C
Extension	20 s at 72 °C

Instrument	Model	Operating conditions
Scanning electron microscope (SEM)	JSM-6360LA, JSM-5300JEOL, JEOL-JFC-1100E Ltd., USA	25KV, 25000X
EDX	JSM-6360LA, JSM-5300JEOL, JEOL-JFC-1100E Ltd., USA	25KV, 25000X
UPLC-MS	Waters ACQUITY UPLC, ESI-MS-XEVO TQD triple quadruple instrument. Waters Corporation, MA01757 U.S.A.	ACQUITY UPLC - BEH C18 1.7 µm – 2.1 × 50 mm Column. Flow rate: 0.2 mL\min
XRD	X'Pert^3 Powder, Netherland.	X-ray tube target: Cu voltage: 40.0 (kV), scan speed = 12.0000 (deg/min)
Thermal analysis	Perkin-Elmer TGA7 Thermobalance	temperature heating range is 20–1000 °C, heating rate is 10 °C min^{-1}

Table 1. Represents the employed techniques for characterizing the structure and their specifications.

Genes	Forward sequence	Reverse Sequence
GAPDH	5´-GTC TCC TCT GAC TTC AAC AGC G-3´	5´-ACC ACC CTG TTG CTG TAG CCA A-3´
BCL-2	5´-ATC GCC CTG TGG ATG ACT GAG T-3´	5´-GCC AGG AGA AAT CAA ACA GAG GC-3´
BAX	5´-TCA GGA TGC GTC CAC CAA GAA G-3´	5´-TGT GTC CAC GGC GGC AAT CAT C-3´

Table 2. LC-QTOF-MS analysis of *Salinicoccus* sp. RM1 extract at ES +ve mode.

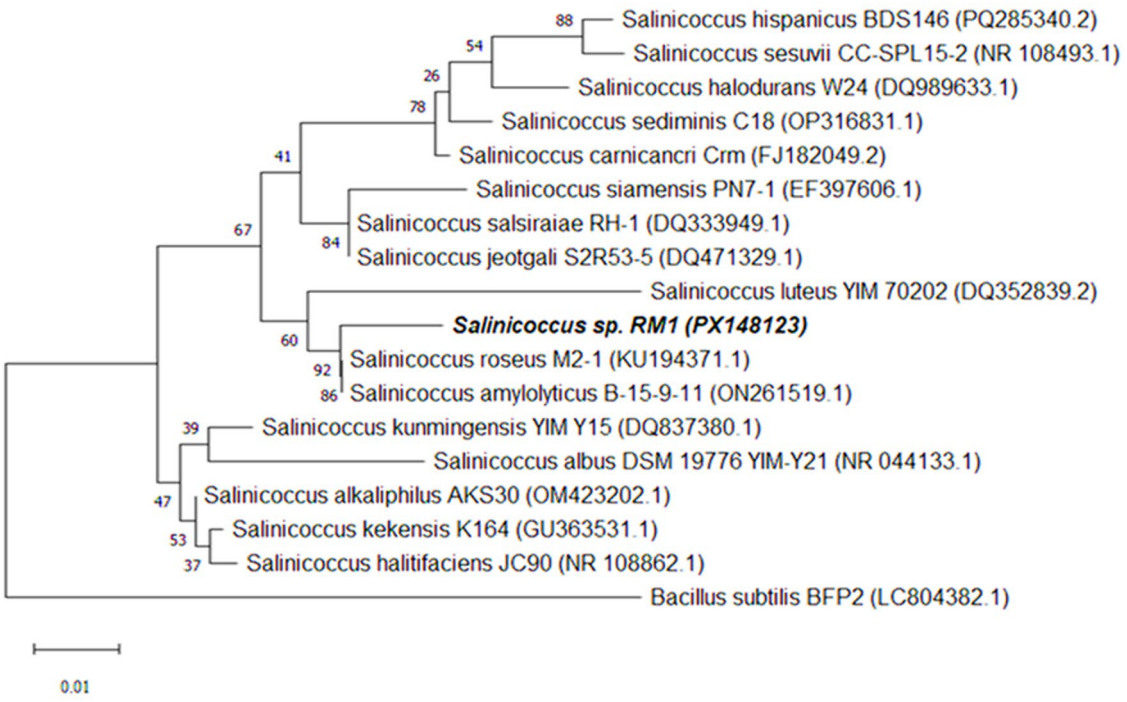

Fig. 1. Phylogenetic tree of *Salinicoccus* sp. RM1. A bold-style typeface was used to designate *Salinicoccus* sp. RM1. The strain names are followed by the GenBank sequence accession numbers. The evolutionary analysis was carried out using the MEGA 11 software program.

The potency of real-time PCR for the selected genes was relatively quantified and normalized by the housekeeping *GAPDH* gene. Both forward and reverse primer sequences are presented in Table 2. Reactions were conducted in triplicate, and the comparative Livak method ($2-\Delta\Delta CT$) was used for data analysis.

Statistical analysis

The measurements were performed in triplicate, and the data are presented as the mean ± SD. SPSS software (version 22.0) was used. Analysis of variance (ANOVA) and Tukey's test were performed with a significance level of $p = 0.05$.

Results and discussion

Isolation, screening, morphological, and molecular identification

In the present investigation, bacteria were isolated from the Red Sea at Rabigh City, Saudi Arabia, purified, and cultured on nutrient agar plates. The colonies typically appear small-sized, circular, and convex with smooth, entire margins. The colonies exhibit a distinct orange-pink non-diffusible pigmentation. Under a microscope, with Gram staining, the cells appeared as Gram-positive, non-sporing cocci. According to the molecular identification and the results of the sequence similarity computations, *S. roseus* M2-1 was our strain's closest relative. The bacterial isolate was given the name *Salinicoccus* sp. RM1 and submitted to GenBank at the NCBI Nucleotide database (Accession Number: PX148123) (Fig. 1).

Salinicoccus sp. RM1 growth conditions

By examining salinity tolerance, pH, and temperature, *Salinicoccus* sp. RM1 was physiologically characterized (Fig. 2). *Salinicoccus* sp. RM1 developed most optimally at 4.5% NaCl and could withstand salinity levels as high as 10% after 39 h; in the absence of NaCl, no development took place (Fig. 2A). While a pH of 9 or 10 resulted in noticeably poor growth, a pH of 7 enabled maximum growth (Fig. 2B). Various temperatures (20–

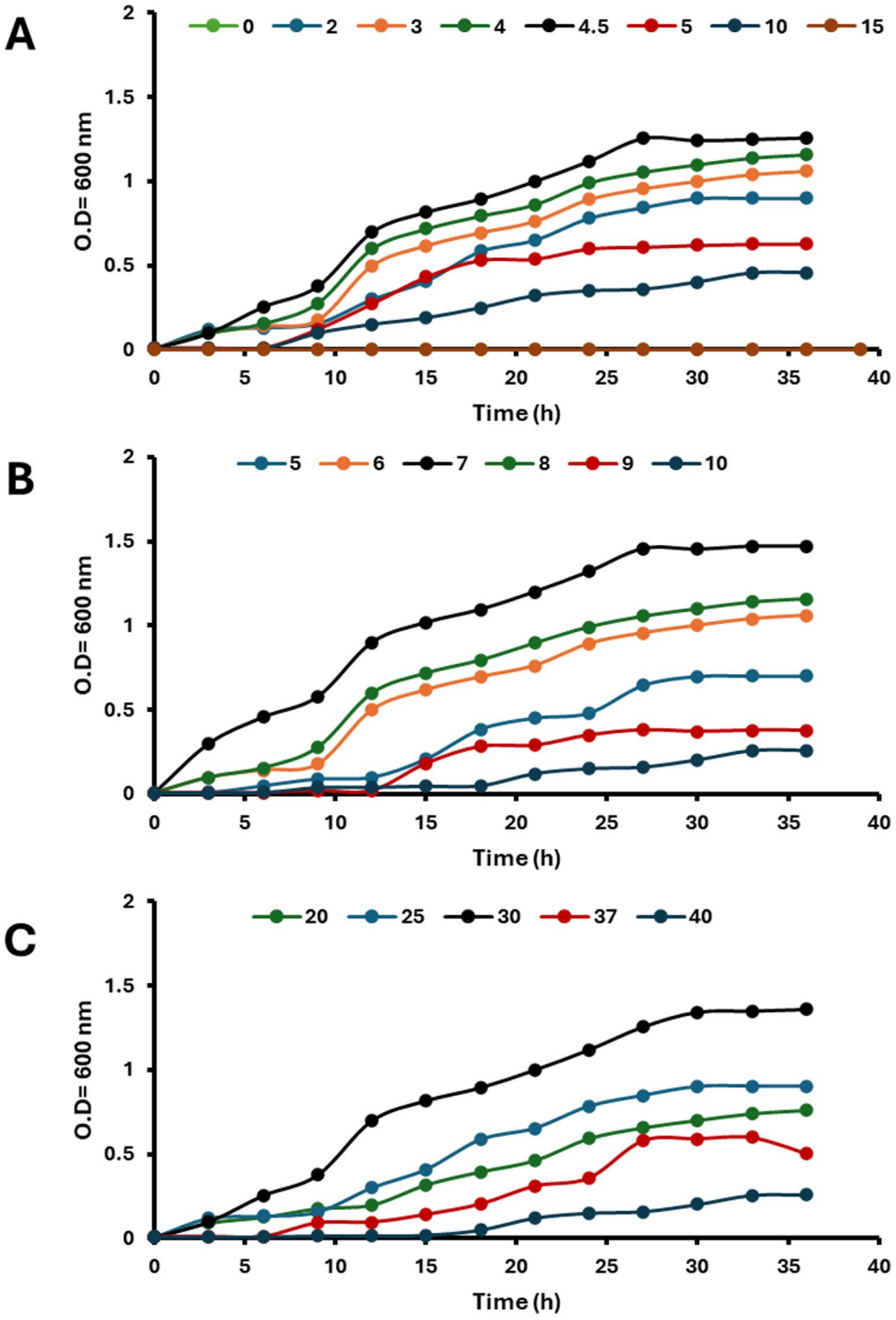

Fig. 2. Growth of *Salinicoccus* sp. RM1 in nutrient broth medium at A different NaCl concentrations at 30 °C and pH = 7; B different pH at 30 °C and 4.5% NaCl; and C different temperatures at pH = 7 and 4.5% NaCl.

37 °C) were found to promote bacterial growth; 30 °C was shown to be the optimal growth temperature, whereas 40 °C was found to impede growth (Fig. 2C). Consequently, the strain's development is dependent on NaCl, and the capacity of *Salinicoccus* sp. RM1 to thrive at a concentration of 4.5% NaCl indicates that they are either moderately halophilic or halotolerant, according to the prior results.

The *Salinicoccus* genus is typically associated with salty habitats, such as salt mines, salted fish, and fermented seafood; therefore, members of this genus vary in the optimum NaCl concentration required for growth[49]. There is a strong correlation between the abundance of *Salinococcus* bacteria in marine habitats and their importance in processes such as the breakdown of aromatic compounds and the biogeochemical cycles of sulfur and carbon[50]. It was reported that marine *S. qingdaonensis* sp. can grow optimally at 3% (w/v) NaCl and pH 8.5[51], while *S.*

kekensis can grow at 8% (w/v) NaCl[52]. The optimum growth of the marine *S. sediminis* was 15% (w/v) at a pH of 8[53]. With a higher NaCl concentration, *S. halitifaciens* and *S. salitudinis* can grow at 10–12% (w/v) NaCl[54,55]. By controlling their osmotic concentrations in environments with high salt content, the halophilic bacteria can use osmolytes, which are solutes that are compatible with them. These osmolytes include carbohydrates, amino acids, polyols, betaines, and ectoines[56].

Characterization of the MK and the prepared NPs

UV spectra

The ultraviolet-visible (UV-Vis) absorption spectrum of *Salinicoccus* sp. RM1 extract offers essential corroborative evidence for the identification of MKs (Fig. 3A). The observation of distinct peaks at 325 nm and 345 nm provides deeper insight into the specific structures present. The longer-wavelength absorptions are significant, as they characterize the influence of the isoprenoid side chain on the chromophore[24]. The absorption in this region indicates the presence of conjugated double bonds in the side chain on the naphthoquinone core. The morphology and configuration of these peaks align with the longer-chain menaquinones (MK-9, MK-10, and MK-13). The spectral data support the conclusion that the primary constituents of this marine bacterial extract are a range of MKs with differing chain lengths, which are crucial for its respiratory function and membrane structure.

(Fig. 3B) The UV–Vis absorption spectrum of pure $CuFe_2O_4$ NPs shows an absorption band around 340 nm, attributed to charge transfer transitions within the spinel lattice, and a sharp peak at 443 and 475 nm related to d–d transitions of Cu^{2+} and Fe^{3+} ions. Confirming the semiconducting nature and good dispersion of the nanoparticles.

(Fig. 3C) represents $CuFe_2O_4$ NPs-MK, the UV–Vis spectrum exhibits an absorption band centered at 340 nm, attributed to MK layer, and a sharp peak at 485 nm related to copper ferrite nanoparticles. These shifts and intensity changes indicate electronic coupling and surface interaction between MK molecules and the $CuFe_2O_4$ surface, suggesting successful conjugation or encapsulation. A slight redshift of the main ferrite band also points to charge transfer or bandgap narrowing due to the organic–inorganic interface.

Proton nuclear magnetic resonance (^{1}H-NMR) spectroscopy

The ^{1}H-NMR spectrum of *Salinicoccus* sp. RM1 extract recorded in $CDCl_3$/DMSO-d_6 shows multiple diagnostic signals (Fig. 4). A sharp singlet at ~ 7.27 ppm corresponds to aromatic protons of the naphthoquinone core. The most intense signal appears at ~ 2.85 ppm, likely corresponding to benzylic methylene protons adjacent to the aromatic ring or allylic positions. A series of multiplets and doublets between 0.5 and 2.5 ppm is characteristic of methyl and methylene protons in the isoprenoid side chain. Signals around 3.85 ppm may suggest the presence of protons near oxygenated or substituted carbons. Interestingly, no clear signals appear in the 5.0–5.5 ppm region, which typically hosts vinyl protons from unsaturated isoprenoids. This suggests that the compound may be a partially hydrogenated MK derivative, such as MK-1, MK-3, MK-5, MK-6, MK-7, and MK-9 (II-H_2), where some double bonds are saturated. The overall pattern is in excellent agreement with the structure of MKs with mid- and long isoprenoid tails[23].

X-ray diffraction (XRD)

Figure 5A, The XRD pattern confirms the production of a spinel-structured crystalline $CuFe_2O_4$ phase. The diffraction peaks at 2θ values of 18.7°, 29.7°, 35.5°, 38.5, 42.7°, 48.4°, and 57.0° correspond to the crystallographic planes (111), (220), (311), (222), (400), (422), and (511) of the face-centered cubic spinel lattice (space group Fd-3 m), which match the standard reference pattern for $CuFe_2O_4$ (JCPDS card No. 25–0283 or 34–0425)[57].

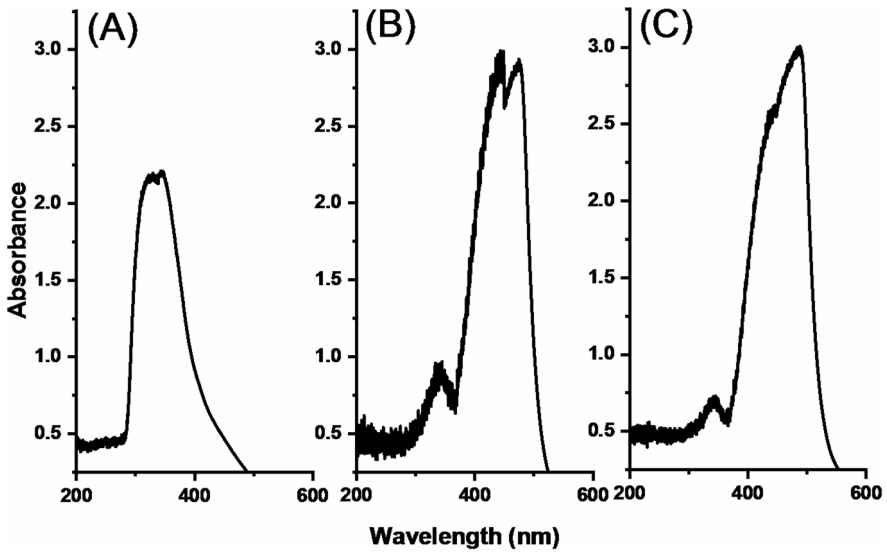

Fig. 3. Ultraviolet-visible (UV-Vis) absorption spectrum of *Salinicoccus* sp. RM1 extract.

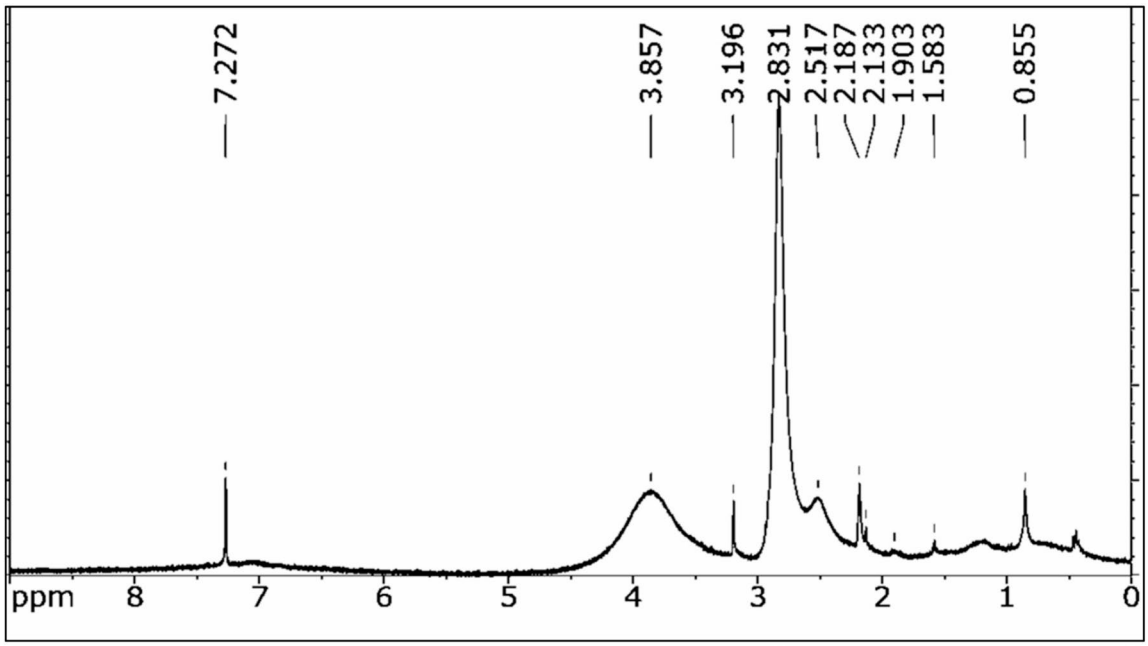

Fig. 4. ^{1}H-NMR spectrum of *Salinicoccus* sp. RM1 extract.

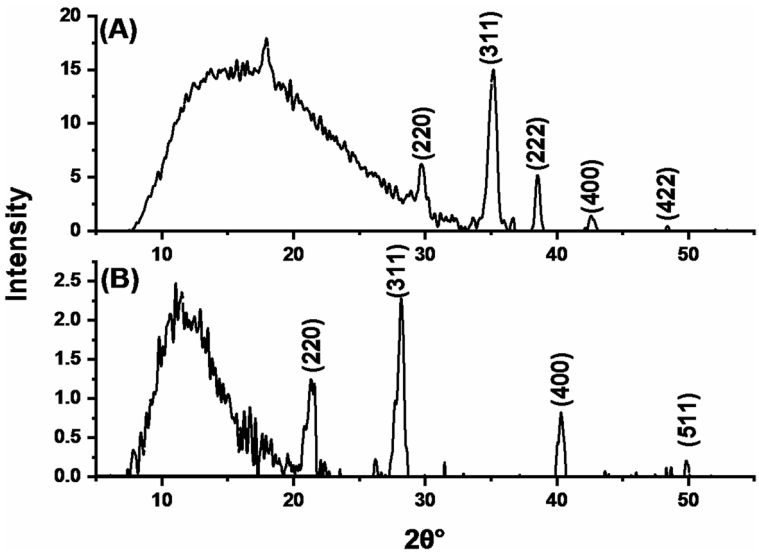

Fig. 5. The X-ray diffraction (XRD) (**A**) $CuFe_2O_4$ NPs, (**B**) $CuFe_2O_4$ NPs-MK.

Successful $CuFe_2O_4$ production is indicated by the intensity and unique nature of the (311) peak at ~ 35.5°, the most intense reflection for the spinel structure. Additionally, the average crystallite size was estimated using the Scherrer equation (Eq. 1), applied to the full width at half maximum (FWHM) of the most intense peak, which was 35 nm[58].

$$D = K/(\cos) \quad (1)$$

Where λ is the wavelength of the Cu-Kα radiation, and β is the full-width at half-maximum (FWHM) intensity in radians. The % Crystallinity is calculated using the following equation[59]:

$$\%\,\text{Crystallinity} = [Ac/(Ac + Aa)] \times 100 \quad (2)$$

Where, Ac: Total integrated area under all the crystalline peaks, and Aa: Total integrated area under the amorphous halo(s). according to Eq. 2 the % crystallinity was 75%[60].

The XRD analysis of $CuFe_2O_4$ NPs-MK (Fig. 5B) indicates that the primary $CuFe_2O_4$ reflections in the composite XRD vary systematically with the MK quantity, resulting in reduced ferrite peak intensities and broadening due to surface coating. Comparing to $CuFe_2O_4$, there are peak shifts as follows: peak (220) from 29.7 to 21.3, peak (311) shifted from 35.5 to 28, peak (222) from 38.5 to 31, peak (422) from 48.4 to 40.3. An amorphous halo at low angles indicates disordered or partially amorphous MKs. Generally, MK decreases the ferrite peak, and the shift suggests that the surface modification, as MK mainly adsorbs without changing the $CuFe_2O_4$ structure.

Infrared spectrum of *Salinicoccus* sp. RM1 MKs & fourier transform infrared of nanocomposite

The infrared spectrum of *Salinicoccus* sp. RM1 MKs (Fig. 6A) reveal different vibrational signatures indicative of MK isoforms MK6-MK9 buried within a complex biological matrix. A notable carbonyl (C = O) stretching at 1655 cm^{-1}, indicative of the quinone moiety in MKs, predominates the mid-IR region, exhibiting a redshift of around 15 cm^{-1} relative to isolated MKs (usually 1670 cm^{-1})[61]. This shift signifies electronic perturbation of the quinone group. Complementary asymmetric and symmetric C–H stretches at 2920 cm^{-1} and 2850 cm^{-1} originate from the polyisoprenyl side chains of MK-6 and MK-9 (comprising 6–9 isoprene units), whereas methylene (CH_2) bending vibrations at 1460 cm^{-1} further substantiate the aliphatic nature of these chains[61]. At 3000–3600 cm^{-1}, the spectra show a large O–H/N–H overlap, indicating hydrogen-bonded water, peptidoglycan hydroxyls, and amine groups from co-extracted biomolecules[61]. Crucially, the absence of sharp nitrate (~1380 cm^{-1}) or sulfate (~1100 cm^{-1}) contaminant peaks suggest effective purification. The complex fingerprint region (1000–1400 cm^{-1}) displays overlapping skeletal vibrations from menaquinone's naphthoquinone ring (C–C/C–O) and contributions from other cellular constituents[61]. The broadening of all major bands, particularly the redshifted C = O band, reflects a heterogeneous microenvironment where MKs interact dynamically with proteins, lipids, and ions consistent with their localization in bacterial membranes. These spectral features collectively confirm the presence of functional groups in the extracted MKs.

The FT-IR spectra of $CuFe_2O_4$ NPs (Fig. 6B) exhibit unique vibrational modes associated with the spinel lattice and surface adsorbates. O–H stretching vibrations of physisorbed water molecules cause a large absorption band at 3400 cm^{-1}, whereas the H–O–H bending mode shows a peak at 1630 cm^{-1}[20]. The fingerprint region below 1000 cm^{-1} indicates spinel structure: a strong band at 570 cm^{-1}, corresponding to the intrinsic stretching of Fe^{3+}–O bonds in tetrahedral coordination (A-sites), and a band at 430 cm^{-1}, resulting from Cu^{2+}–O and Fe^{3+}–O vibrations in octahedral coordination. Weak peaks observed between 1380 and 1450 cm^{-1} may be caused by residual nitrate groups from precursors or ambient carbonate species on high-surface-area nanoparticles[10]. The $CuFe_2O_4$ NPs produced is phase pure, as there are no organic functional group vibrations above 1500 cm^{-1}. This provides a framework for additional functionalization studies.

$CuFe_2O_4$ NPs-MK has considerable FT-IR spectra changes (Fig. 6C), indicating surface loading and molecular interaction. The spinel core is preserved in the low-frequency area, where typical Fe^{3+}–O (tetrahedral, ~ 570 cm^{-1}) and Cu^{2+}/Fe^{3+}–O (octahedral, ~ 430 cm^{-1}) vibrations are present. However, the organic layer dampens these bands, resulting in reduced intensity and widening. New MKs fingerprints reveal a distinct carbonyl (C = O) stretch at 1655 cm^{-1}, redshifted by approximately 15 cm^{-1} from the free MKs. This suggests potential coordination or hydrogen bonding between the quinone oxygen and surface metal ions (Fe^{3+}/Cu^{2+})[62]. The asymmetric and

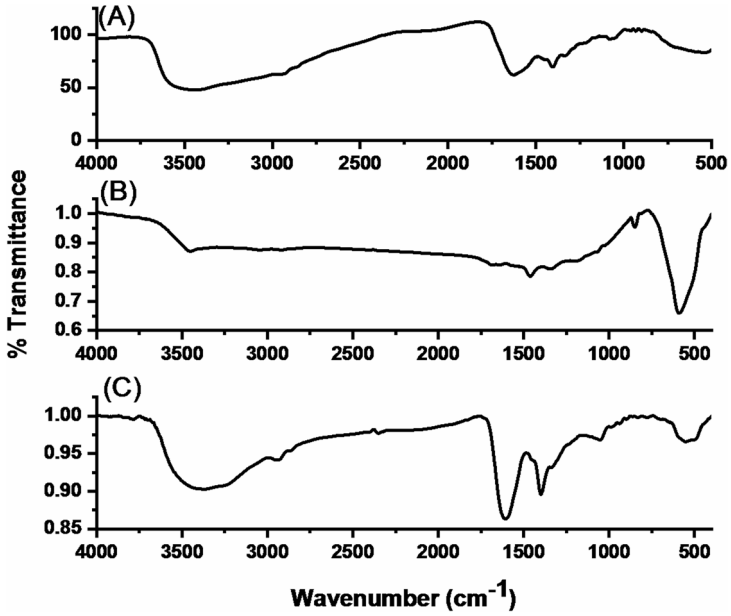

Fig. 6. (**A**) Infrared spectrum of the *Salinicoccus* sp. RM1 extract, (**B**) FT-IR of $CuFe_2O_4$ NPs, and (**C**) $CuFe_2O_4$ NPs-MK.

symmetric C–H stretching vibrations of the polyisoprenyl chain appear as separate peaks at 2920 cm^{-1} and 2850 cm^{-1}, respectively, whereas methylene (CH_2) bending modes are observed around 1460 cm^{-1}[61]. The MK structure is characterized by overlapping C–C skeletal vibrations, C–O stretches, and methyl deformations in the fingerprint region, spanning 1000–1400 cm^{-1}. The O–H stretching band (~ 3400 cm^{-1}) broadens asymmetrically towards lower wavenumbers, indicating stronger hydrogen bonding between the surface hydroxyl groups of MKs, adsorbed water, and polar functional groups, which confirms the surface coverage of MK-6, MK-7, and MK-9. The spectrum changes reveal chemisorption via quinone-metal coordination and hydrophobic interactions of the isoprenoid chain.

Magnetic analysis of $CuFe_2O_4$ NPs

The magnetic susceptibility analysis of $CuFe_2O_4$ NPs reveals a substantial mass-specific susceptibility $X_B = 272.056 \times 10^{-6}$ cgs at 32.5 °C, indicative of pronounced ferrimagnetic behavior. This elevated value significantly surpasses baseline paramagnetic responses and aligns with characteristic features of spinel ferrites, where uncompensated antiparallel spin alignment in the crystal lattice generates strong intrinsic magnetization[63].

Scanning electron microscopy

Scanning electron microscopy (SEM) analysis provides critical insights into the morphological characteristics of both the synthesized $CuFe_2O_4$ NPs and their composites with MK. Images in Fig. 7A and B depict the pure $CuFe_2O_4$ NPs. Figure 7A, acquired at a relatively low magnification (100X), offers an overview of the sample, revealing the general distribution and potential large-scale aggregation tendencies of the nanoparticle powder. In striking contrast, Fig. 7B, captured at high magnification (30,000X), resolves the primary particles with exceptional detail. This high-resolution view confirms the successful synthesis of $CuFe_2O_4$ NPs, revealing predominantly spherical or near-spherical morphologies. Highlights the presence of some interparticle sintering or aggregation, a common phenomenon in high-surface-area nanomaterials, despite the individual nanoparticles being clearly discernible at this scale.

Figure 7C and D illustrate the $CuFe_2O_4$ NPs-MK. Figure 7C (100X), analogous to Fig. 7A, provides a macroscopic view of the composite material. This view suggests potential differences in bulk morphology or particle packing compared to the pure nanoparticles, possibly indicating the formation of larger composite structures or a more cohesive matrix due to the incorporation of MKs. The transformative effect of MK loading is dramatically evident in Fig. 7D (20,000 X). This high-magnification image reveals that the $CuFe_2O_4$ NPs are effectively loaded with the MKs matrix. The MKs appear as a continuous, often amorphous or film-like phase that coats and bridges individual nanoparticles, forming a cohesive composite architecture. This intimate association between the ferrite nanoparticles and the organic MKs host matrix is crucial, as it demonstrates successful composite formation and suggests potential interactions at the interface, which are highly relevant for the anticipated functionality where synergy between the inorganic and organic components is essential. The SEM analysis collectively confirms the nanoscale nature of the synthesized $CuFe_2O_4$ NPs, reveals their inherent tendency to aggregate, and unequivocally demonstrates the successful formation of a $CuFe_2O_4$ NPs-MK composite material, where the nanoparticles are uniformly integrated within an MK host.

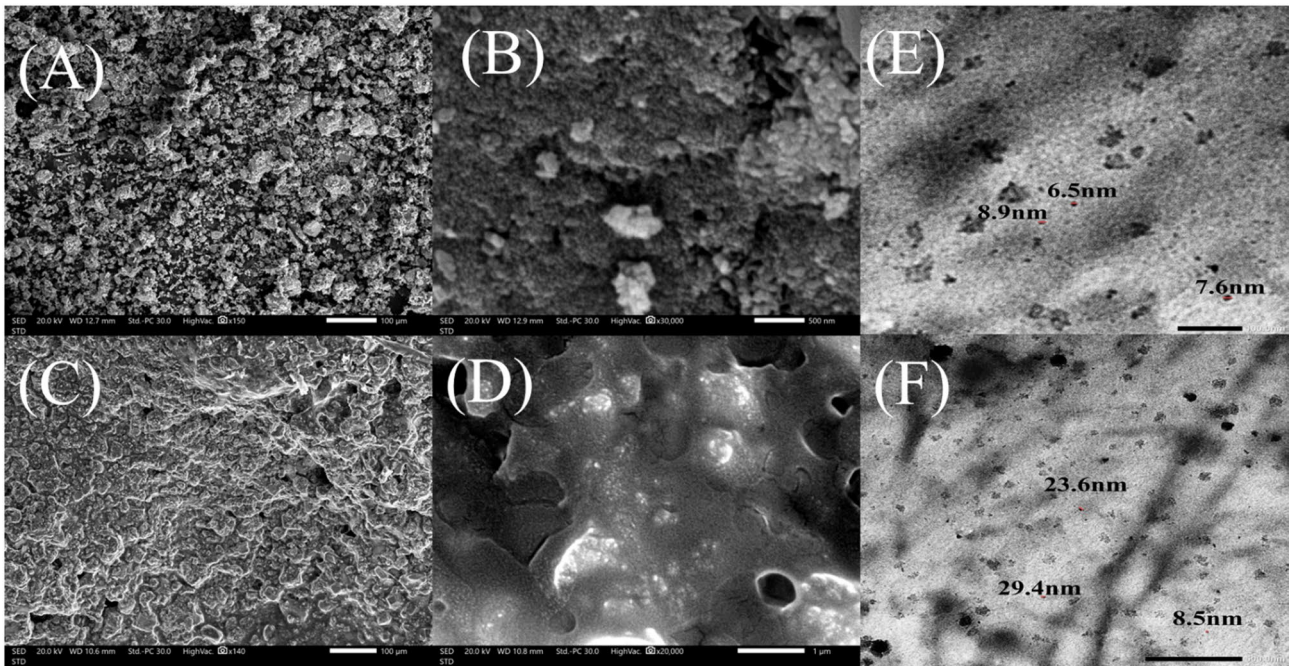

Fig. 7. Scanning Electron Microscopy (SEM) (**A&B**) $CuFe_2O_4$ NPs, (**C&D**) $CuFe_2O_4$ NPs-MK, (**E&F**) TEM of $CuFe_2O_4$ NPs and $CuFe_2O_4$ NPs-MK.

Transmission electron Microscopy

Figure 7E, The TEM image of $CuFe_2O_4$ NPs displays a nearly spherical morphology with a homogeneous dispersion of particles. The measured particle sizes vary from around 6.5 to 8.9 nm, signifying nanoscale dimensions and excellent size uniformity. The fine dispersion and small particle size indicate efficient synthesis and significant potential for elevated surface area, therefore expanding their catalytic and adsorption characteristics.

The TEM image of $CuFe_2O_4$ NPs-MK (Fig. 7F) shows nanoparticles with a slightly larger and more variable size distribution compared to pure $CuFe_2O_4$. The observed particle sizes range between 8.5 and 29.4 nm, indicating partial aggregation and possible interaction between $CuFe_2O_4$ NPs and the MKs. The image reveals a semi-spherical morphology with good dispersion, suggesting successful incorporation of $CuFe_2O_4$ into the MK structure while maintaining nanoscale features favorable for enhanced surface reactivity and stability.

Energy dispersive X-ray

Energy dispersive X-ray (EDX) spectroscopy provides essential elemental composition data for the $CuFe_2O_4$ NPs and their MK composites, corroborating structural and compositional differences between the two systems. The EDX spectrum of the pure $CuFe_2O_4$ NPs (Fig. 8A) reveals a predominantly inorganic composition dominated by iron and copper, with oxygen constituting. The atomic percentages closely align with the theoretical 2:1 stoichiometry of $CuFe_2O_4$ (Fe/Cu atomic ratio = 2.0). The minimal carbon content suggests limited organic contamination consistent with an unmodified inorganic nanoparticle system.

In contrast, the EDX analysis of the $CuFe_2O_4$ NPs-MK (Fig. 8B) reveals a significantly transformed elemental profile, confirming the successful functionalization of the nanoparticles. A substantial carbon signal accompanied by the emergence of nitrogen, both signature elements of the organic MKs matrix. Additionally, the iron, copper, and oxygen peaks remain detectable; their relative intensities decrease due to dilution within the organic phase. Confirming retention of the nanoparticle's core composition after MK integration. Additional elements, including sodium and potassium, are present due to the support of the $CuFe_2O_4$ NPs-MK on the glass slide for analysis. This elemental analysis verifies the composite nature, demonstrating the coexistence and integration of the inorganic $CuFe_2O_4$ phase within an organic MK. EDX provides direct chemical evidence supporting the morphological observations from SEM analysis.

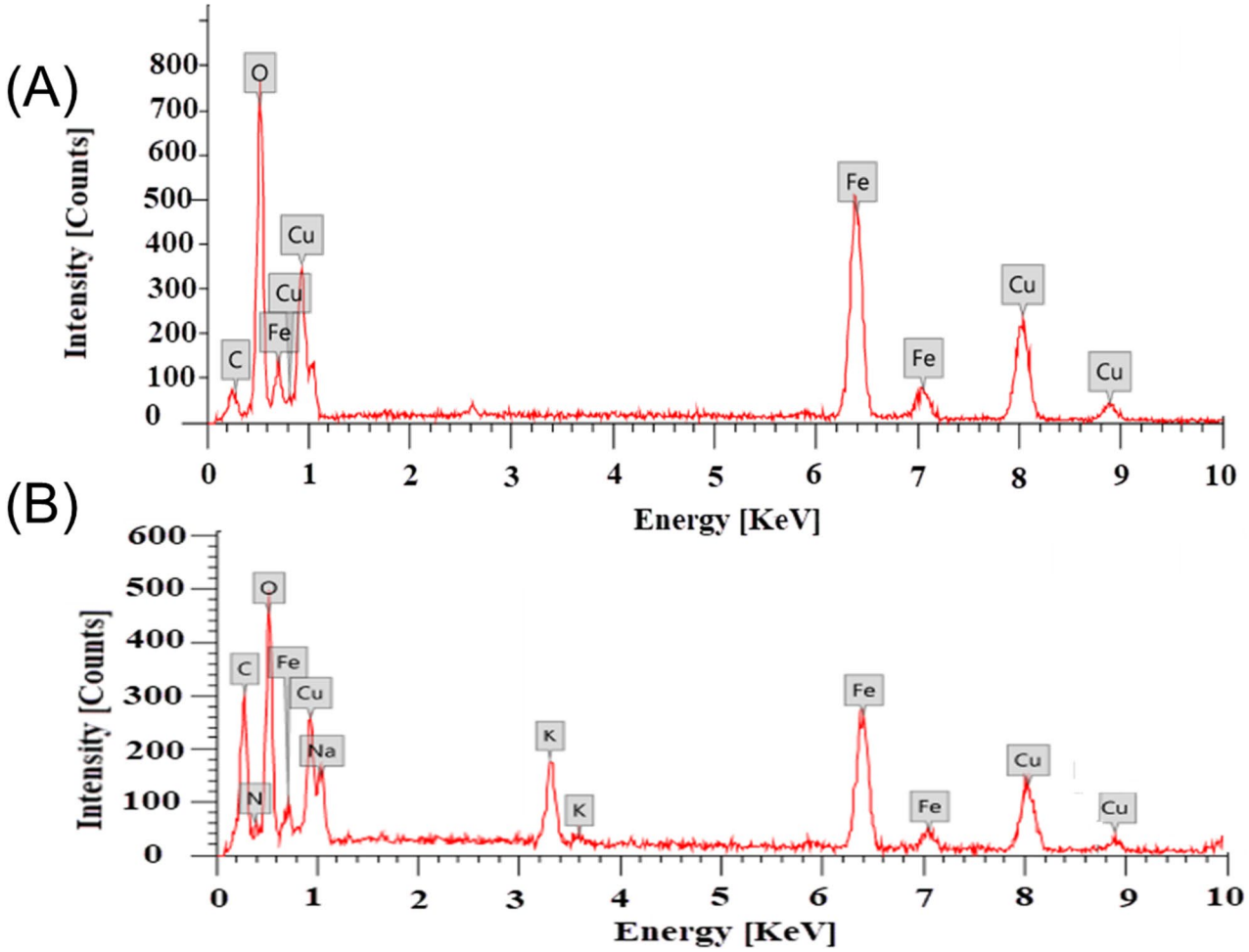

Fig. 8. Energy Dispersive X-ray (EDX) (**A**) $CuFe_2O_4$ NPs, (**B**) $CuFe_2O_4$ NPs-MK.

Particle size analysis (PSA)

The particle size analysis of $CuFe_2O_4$ NPs (Fig. 9A) reveals a well-distributed nanoscale range with a median diameter (D50) of approximately 113 nm, indicating the successful synthesis of fine particles. The moderate polydispersity (PDI = 0.688) indicates controlled size variation, making it suitable for multifunctional applications. Overall, the data demonstrate effective formation of stable $CuFe_2O_4$ NPs with consistent dispersion characteristics. The $CuFe_2O_4$ NPs-MK (Fig. 9B) displays a uniform nanoscale distribution with a median particle size of 155 nm and two well-defined peaks at 80 and 223 nm, confirming successful menaquinone loading. The very low PDI (0.0449) indicates excellent homogeneity and stable particle dispersion, making it suitable for biomedical applications.

Surface area analysis

The surface area, pore volume, and pore radius of $CuFe_2O_4$ NPs were assessed using several analytical techniques. The BET technique indicated a surface area of 55.12 m^2/g. The Langmuir technique produced a surface area of 237.56 m^2/g, whereas BJH adsorption and desorption resulted in surface areas of 98.75 m^2/g and 139.31 m^2/g, with pore volumes of 0.470 cm^3/g and 0.491 cm^3/g, and pore radii of 2.27 nm and 1.68 nm, respectively. The DH adsorption and desorption techniques measured surface areas of 103.13 m^2/g and 145.50 m^2/g, pore volumes of 0.466 cm^3/g and 0.487 cm^3/g, and pore radii of 2.27 nm and 1.68 nm. The DFT approach revealed a surface area of 141.85 m^2/g, a pore volume of 0.465 cm^3/g, and a pore radius of 6.28 nm, whereas the DR method determined a micropore surface area of 355.08 m^2/g, a micropore volume of 0.127 cm^3/g, and a pore radius of 2.79 nm.

The surface area, pore volume, and pore radius of $CuFe_2O_4$ NPs modified with MK were assessed using various methodologies. The BET approach indicated a surface area of 38.63 m^2/g, whereas the Langmuir method documented 152.26 m^2/g. The BJH adsorption and desorption techniques produced surface areas of 65.03 m^2/g

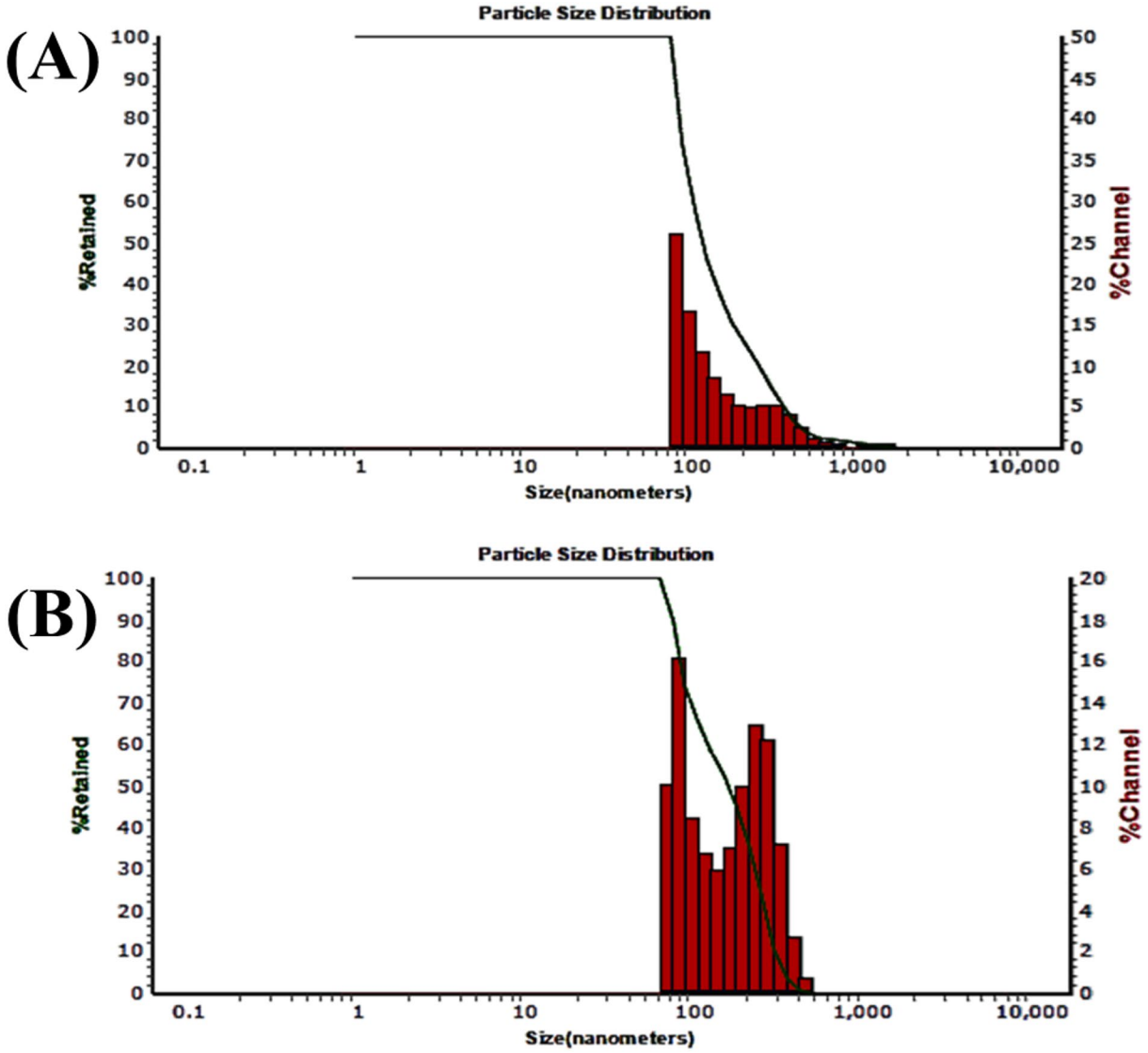

Fig. 9. Particle size analysis of (**A**) $CuFe_2O_4$ NPs and (**B**) $CuFe_2O_4$ NPs-MK.

and 90.45 m^2/g, with associated pore volumes of 0.339 cm^3/g and 0.350 cm^3/g, and pore radii of 2.28 nm and 5.69 nm, respectively. The DH adsorption and desorption techniques yielded surface areas of 67.79 m^2/g and 94.22 m^2/g, pore volumes of 0.335 cm^3/g and 0.347 cm^3/g, and pore radii of 2.28 nm and 5.69 nm, respectively. The DFT approach revealed a surface area of 93.11 m^2/g, a pore volume of 0.327 cm^3/g, and a pore radius of 6.28 nm. The results validate the mesoporous characteristics of the $CuFe_2O_4$ NPs-MK composite. The $CuFe_2O_4$ NPs-MK sample had a reduced BET surface area relative to the pure $CuFe_2O_4$ NPs, suggesting partial surface occlusion by the MK component. This reduction indicates that MK inclusion somewhat diminishes surface accessibility while preserving a mesoporous shape conducive to adsorption and catalytic activity.

LC-ESI-QTOF-MS analysis of *salinicoccus* sp. RM1 MK

Comprehensive LC-QTOF-MS analysis of *Salinicoccus* sp. RM1 MK was performed under both positive (ES^+), Fig. 10A, and negative (ES^-), Fig. 10B, conditions, demonstrating electrospray ionization modes that characterized the menaquinone homologues present. The retention times, observed m/z values, and compound assignments are summarized in Fig. 10.

In ES^+ mode (Table 3), nine distinct signals were observed over a chromatographic window of 0–20 min. A peak at 0.69 min with m/z 301.1410 corresponded to menadione (vitamin K_3), indicating the presence of a low-molecular-weight quinone fragment or biosynthetic intermediate. Higher homologues were clearly resolved, with MK-4 (m/z 445.3182, 5.58 min), MK-5 (m/z 513.3828, 6.46 min), MK-7 (m/z 649.5039, 11.35 min), MK-8 (m/z 717.5662, 13.60 min), MK-9 (m/z 785.6285, 15.33 min), MK-10 (m/z 853.6908, 16.24 min), MK-12 (m/z 989.8154, 17.92 min), and MK-13 (m/z 1057.8776, 19.64 min) detected in succession. This pattern reflects the biosynthesis of long-chain polyprenylated quinones, which are typically associated with Gram-positive bacteria, including those found in marine environments. The progressive increase in retention time with longer isoprenoid chains is consistent with their increasing hydrophobicity[64].

In ES^- mode (Table 4), the early part of the chromatogram (0.5–0.7 min) contained a cluster of signals indicative of structurally related MKs and their oxidative or degraded derivatives. A signal at 0.516 min (m/z 541.2509) was assigned to MK-4 or a closely related derivative, while m/z 557.2253 (0.517 min) represented an oxidized MK-4 species. Two overlapping peaks at m/z 585.2153 and m/z 601.1894 were assigned to MK-7 and

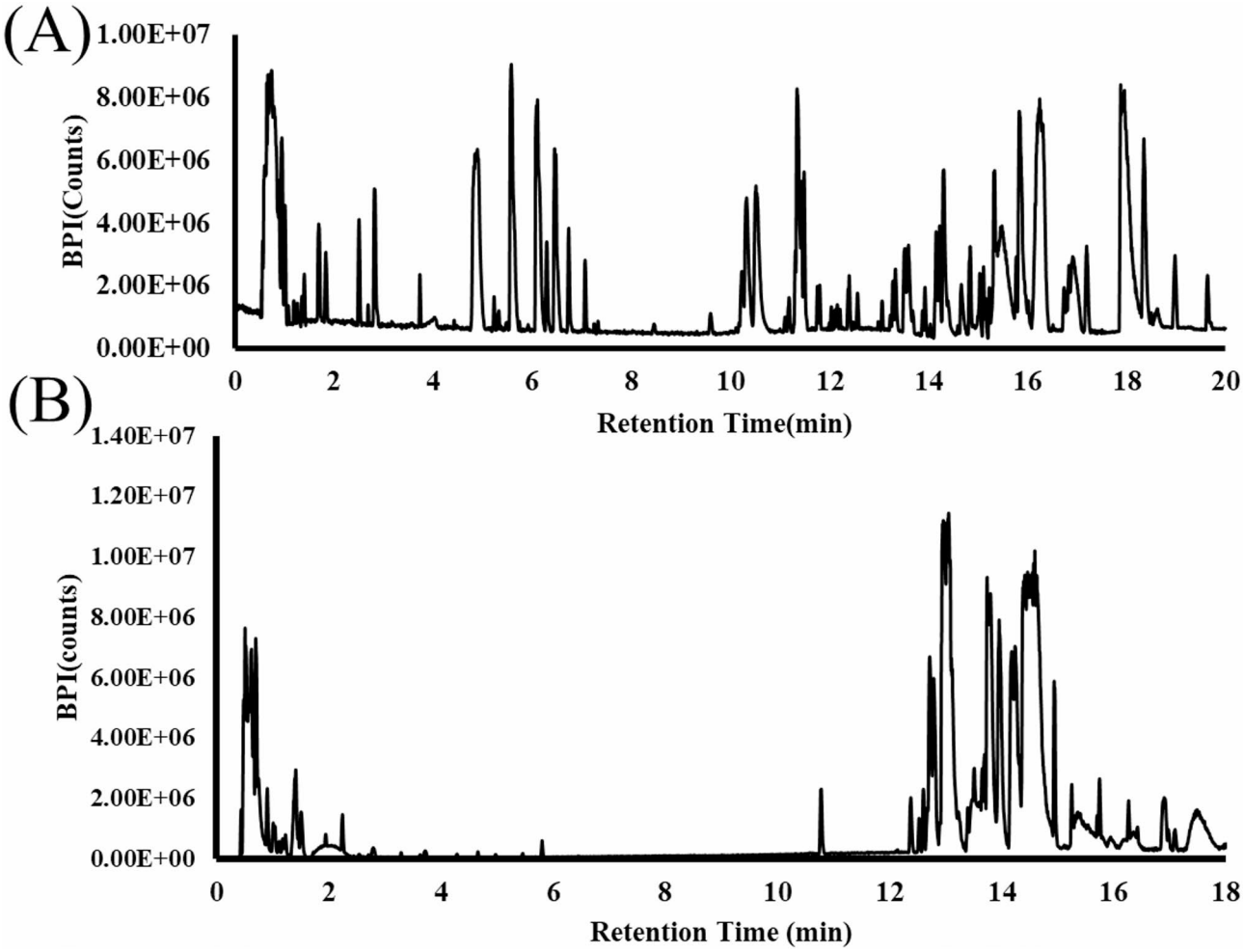

Fig. 10. LC-QTOF-MS analysis of *Salinicoccus* sp. RM1 extract (**A**) ES+ve mode and (**B**) ES-ve mode.

Retention Time (min)	Observed m/z	Suggested Compound
0.69	301.1410	**Menadione (K3)**
5.58	445.3182	**MK-4 (K2-4)**
6.46	513.3828	**MK-5 (K2-5)**
11.35	649.5039	**MK-7 (K2-7)**
13.60	717.5662	**MK-8 (K2-8)**
15.33	785.6285	**MK-9 (K2-9)**
16.24	853.6908	**MK-10 (K2-10)**
17.92	989.8154	**MK-12 (K2-12)**
19.64	1057.8776	**MK-13 (K2-13)**

Table 3. LC-QTOF-MS analysis of *Salinicoccus* sp. RM1 extract at ES +ve mode.

Retention Time (min)	Observed m/z	Suggested Compound
0.516	541.2509	MK-4 or derivative
0.517	557.2253	Oxidized MK-4
0.517	585.2153	**MK-7**
0.517	601.1894	MK epoxide
0.603	585.2147	**MK-7** (confirm)
0.607	579.2060	MK-5 or degraded form
0.610	557.2190	MK-4 derivative
0.610	541.2504	MK-4 related
14.944	797.874	**MK-10**
15.747	782.650	**MK-8**

Table 4. LC-QTOF-MS analysis of *Salinicoccus* sp. RM1 extract at ES -ve mode.

the MK epoxide form, respectively. Additional confirmation of MK-7 was provided by a second peak at 0.603 min (m/z 585.2147). Minor signals at m/z 579.2060 (0.607 min) and m/z 557.2190 (0.610 min) suggested the presence of MK-5 or degraded MK-4 derivatives, while m/z 541.2504 (0.610 min) indicated another MK-4-related ion. In the later retention range, two prominent peaks were detected at 14.944 min (m/z 797.874, MK-10) and 15.747 min (m/z 782.650, MK-8), corresponding to longer-chain MKs that were also observed in ES^+ mode[23].

The combined ES^+ and ES^- profiles confirm that the marine bacterial methanolic extract predominantly contains long-chain MKs (MK-7 through MK-10, MK-12, and MK-13), which are typical for many halophilic species. The detection of menadione (K_3) at an early retention time suggests active quinone biosynthesis, as menadione is a known precursor in the pathway toward fully prenylated menaquinones. The presence of oxidized and epoxide derivatives in ES^- mode indicates either in vivo oxidative modifications or in vitro degradation during extraction and analysis. The dominance of MK-7, MK-8, MK-9, and MK-10 aligns with previous reports of MK profiles in marine actinomycetes and halophilic cocci, which often exhibit a mixed distribution of mid- to long-chain homologues[65]. These quinones are essential components of the bacterial electron transport chain and can serve as chemotaxonomic markers for species identification[66]. The broad spectrum of MKs, along with their oxidized forms, reflects the organism's metabolic adaptation to a saline marine environment, where respiratory flexibility is advantageous.

Anti-breast cancer effect on *BAX* and *BCL-2* gene expression in MCF-7 cells

Cytotoxicity of $CuFe_2O_4$ NPs-MK

The effect of $CuFe_2O_4$ NPs-MK on MCF-7 cells' growth was illustrated by the viability assay (Fig. 11A), and dose-response data were generated (Fig. 11B**).** At the lowest concentrations tested (3.9 and 7.8 µg/ml), the compound exhibits minimal toxicity, with effects barely above a baseline level of approximately 6%. As the concentration increases, the effect begins to accelerate markedly; between 15.6 µg/ml and 125 µg/ml, the toxicity percentage rises steeply from 15.65% to 97.88%, indicating a period of highly sensitive response where each doubling of concentration produces a substantial increase in cell death. This is followed by a plateau effect at the highest concentrations (250 to 1000 µg/ml), where the toxicity reaches its maximum efficacy of nearly 100%, and further increases in dose yield no significant additional effect. The most critical of these is the IC_{50} value, which is the half-maximal inhibitory concentration. This value, calculated to be approximately 48.94 µg/ml, represents the potency of the compound and the concentration required to achieve 50% toxicity in the cell population.

In general, $CuFe_2O_4$ NPs exert anti-cancer effects through several mechanisms. They induce lethal oxidative stress by using released copper and iron ions to convert the tumor's hydrogen peroxide into toxic radicals that damage cells[67]. Additionally, they disrupt the cell's energy production (TCA cycle), leading to a toxic buildup of damaged proteins that triggers cell death[68–70]. Furthermore, the ferrimagnetic property of $CuFe_2O_4$ NPs enables

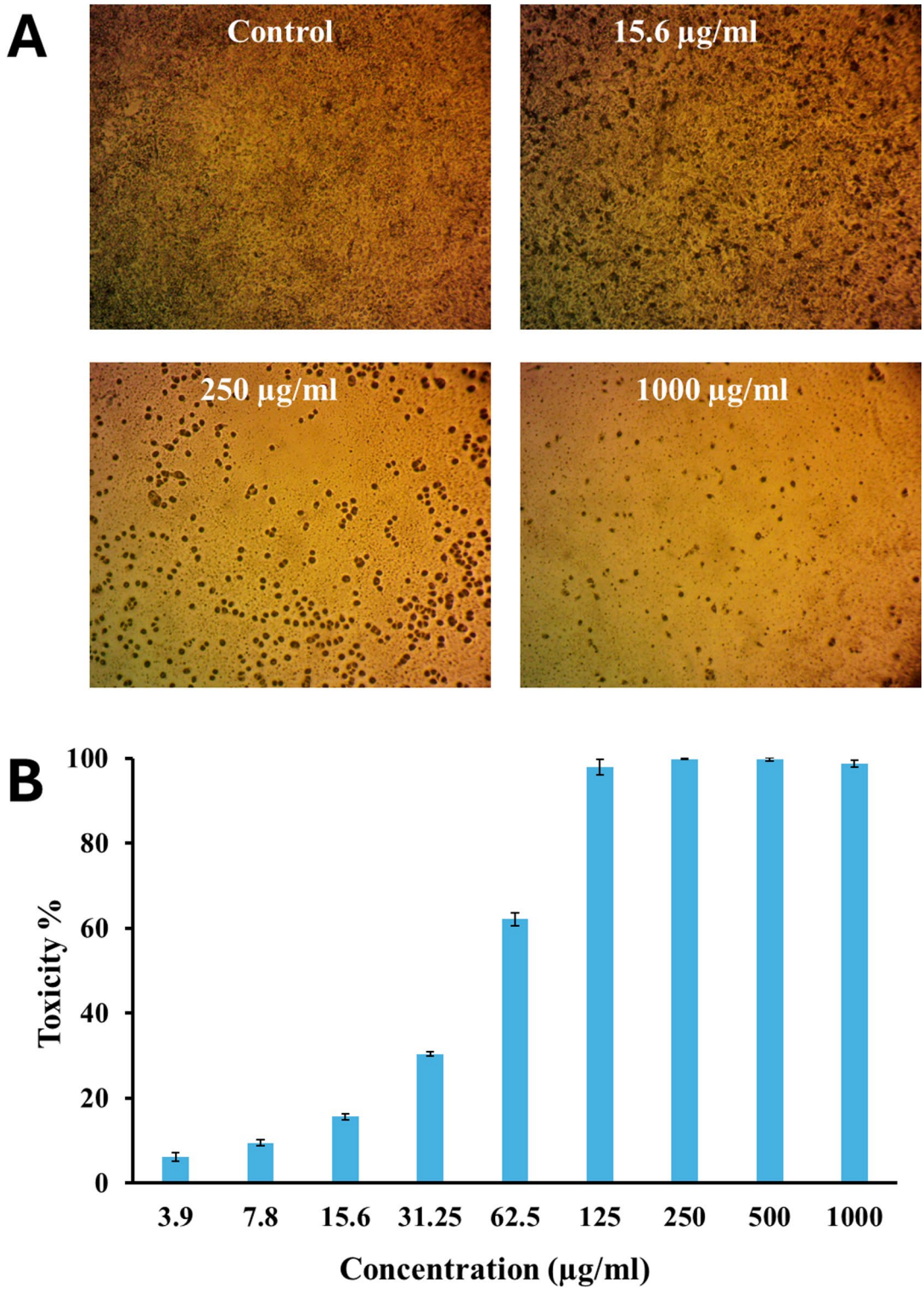

Fig. 11. Cytotoxicity of $CuFe_2O_4$ NPs-MK against MCF-7. Microscope imaging (**A**), dose–response (**B**), mean ± SD $_{(n=3)}$ is represented in the data.

magnetic hyperthermia, generating localized heat that can directly denature cellular proteins and structures, causing the ablation of cancer cells when an external magnetic field is applied[70]. As drug carriers, they enable combined chemo-photothermal therapy, where near-infrared light triggers both drug release and localized heating, resulting in synergistic attack[71]. In summary, $CuFe_2O_4$ NPs kill or inhibit cancer cells through ROS-mediated oxidative stress, induction of apoptosis, enhanced effects when doped, and by augmenting other therapies, such as radiotherapy.

Gene				
GAPDH	Average Cq	ΔCq	ΔΔCq	2^(-ΔΔCq)
– Control	15.395			
– Treated	14.940			
BAX				
– Control	26.883	11.488	0.048	1.034
– Treated	26.380	11.440		
BCL2				
– Control	25.625	10.230	0.858	0.55
– Treated	26.027	11.088		

Table 5. Quantitative PCR (qPCR) analysis data.

Material	Cancer Cell Lines	Reference
$CuFe_2O_4$ NPs–MK	MCF-7	This work
$CuFe_2O_4$@BSA-FA-CUR	MCF-7	[32]
Dy-doped $CoFe_2$-xDy_xO_4, coated with HPGCD	MCF-7 and A375	[31]
Fe_3O_4@ZnO Fe_3O_4@SiO_2 NCs	MCF-7	[30]
$CuFe_2O_4$ decorated with BSA	U-87 cells	[29]
$CuCexFe_2$-xO_4	MCF-7	[28]
Gold nanoparticles	MCF-7	[67]

Table 6. Fabricated Nanoparticles with anticancer activity.

Real-time PCR assay

Based on quantitative PCR (qPCR) analysis, the effect of $CuFe_2O_4$ NPs-MK on gene expression is represented by the changes in *BAX* and *BCL-2* expression, as determined through key calculations that involved normalizing to the *GAPDH* housekeeping gene and calculating the fold change. Cq values were determined, and subsequently, gene expression changes were calculated (Table 5**).** It was observed that there is an increase in *BAX* (pro-apoptotic) expression (1.03-fold), which is very slight based on this data (3.4%). BAX protein promotes cell death by permeabilizing the mitochondrial membrane. An increase, even a small one, pushes the cell towards apoptosis.

Additionally, the decrease in BCL-2 (an anti-apoptotic protein) expression (0.55-fold) is the most significant finding. BCL-2 protein acts as a guardian of the mitochondria, inhibiting cell death[72]. A 45% reduction in its levels severely impedes the cell's ability to suppress apoptosis. The balance between these two proteins is more important than the absolute level of either one. The BAX/BCL-2 ratio is a key indicator of cellular commitment to apoptosis, which was found to be 1.88; this near-doubling of the BAX/BCL-2 ratio strongly suggests that $CuFe_2O_4$ NPs-MK treatment shifts the balance in favor of programmed cell death. The pro-apoptotic mechanism of $CuFe_2O_4$ NPs-MK demonstrates a clear and mechanistically sound anti-cancer effect by targeting the intrinsic (mitochondrial) pathway of apoptosis. It downregulates the protective shield (*BCL-2*) and slightly upregulates the executioner (*BAX*).

Additionally, altering the BAX/BCL-2 ratio is a primary goal of many modern anti-cancer therapies. A key limitation of this study is the reliance on gene expression data (BAX/BCL-2 ratio) from the MCF-7 cell line to infer apoptotic activity without subsequent protein-level or functional validation. While alterations in mRNA levels of these key regulators are a strong indicator of apoptotic initiation, they do not conclusively prove the execution of cell death. The absence of Western blot analysis for BAX/BCL-2 protein expression or functional assays such as Annexin V/PI staining means that the precise anti-cancer mechanism remains to be fully elucidated. Future studies will prioritize these confirmatory experiments to solidify the proposed mechanism of apoptosis induction.

Our findings align with several studies that have reported gene expression changes in MCF-7 cells following exposure to various compounds. Gold NPs upregulated pro-apoptotic *BAX* and down-regulated *BCL-2*[73]. Additionally, natural compounds such as carvacrol and Dioscorea extract induced the upregulation of Bax expression and downregulation of *BCL*−2 gene expression[74,75]. In conclusion, a compound that can effectively lower *BCL-2* levels is highly promising, as *BCL-2* is overexpressed in many cancers, including breast cancer, which renders them resistant to cell death[70]. This is achieved in our study of the $CuFe_2O_4$ NPs-MK effect on gene expression in MCF-7. Additionally, our work was compared to similar studies, as shown in Table 6, to demonstrate the efficiency of our approach.

Safety and efficacy of $CuFe_2O_4$ NPs–MK composites

The $CuFe_2O_4$ NPs-MK system differs from other nanoparticle drug composites due to the synergistic bioactivity of bacterial menaquinones (MKs). To improve solubility, biodistribution, and controlled release, traditional

nanoparticle drug formulations load small-molecule chemotherapeutics (e.g., doxorubicin, paclitaxel) or gene therapeutics onto liposomes, polymeric micelles, mesoporous silica, or metal oxide carriers[76–80]. These methods utilize nanoparticles as passive carriers or triggerable release platforms, and drugs as active cytotoxic agents. Instead, the addition of MKs with biological activity (e.g., redox and mitochondrial pathway regulation) may have both intrinsic therapeutic impact and a payload. Unlike composites, where the carrier is inactive and the therapeutic impact depends only on the drug load, this dual activity may improve efficacy with lower nanoparticle burdens.

For safety, many nanoparticle-drug combinations must address issues related to carrier toxicity and biocompatibility. Researchers suggest that nanoparticles made of iron oxide or ferrite can damage healthy cells by generating reactive oxygen species or undergoing ion leaching[81]. Using pure $CuFe_2O_4$ nanoparticles alone was found to be lethal in CCO (crab cell line) cells, raising concerns about their biocompatibility[82]. In other ferrite systems, such as those containing cobalt or zinc, surface coatings and modifications can reduce genotoxicity and oxidative stress in non-cancerous cells[83]. The use of bacterial MKs as a coating or corona may reduce the toxicity of bare ferrite cores by creating a biomimetic barrier that protects cells from direct contact with reactive surfaces.

Conclusion

In conclusion, this study successfully demonstrates the synthesis of copper ferrite nanoparticles ($CuFe_2O_4$ NPs) functionalized menaquinones (MKs) extracted from the marine bacterium *Salinicoccus* sp. RM1 ($CuFe_2O_4$ NPs-MK). LC-QTOF-MS analysis of MKs revealed that they are rich in long-chain MK homologs. Comprehensive characterization of $CuFe_2O_4$ NPs and $CuFe_2O_4$ NPs-MK, performed via XRD, FT-IR, EDX, SEM, magnetic analysis and particle size analysis verified the successful formation and functionalization of the nanoparticles. The gene expression results provide a strong mechanistic rationale for the anti-cancer effect of $CuFe_2O_4$ NPs-MK, as it successfully targets the mitochondrial apoptosis pathway by crippling the cell's primary survival signal (*BCL-2*) and promoting a cell death signal (*BAX*). This study was designed as an initial investigation to identify promising gene expression signatures. The significant modulation of the BAX/BCL-2 ratio provides a robust rationale for a deeper mechanistic inquiry. Consequently, our future work will directly address this limitation by quantifying the protein expression of these and other apoptotic markers, and by employing functional assays to confirm and quantify the induction of programmed cell death visually. The next immediate step is to confirm the induction of apoptosis at both the protein and functional levels using Western blot analysis for BAX, BCL-2, and cleaved caspase-3, as well as flow cytometry with Annexin V/PI staining.

Furthermore, expanding this research to a panel of cancer cell lines, including other breast cancer subtypes (e.g., MDA-MB-231) and cancers from different tissues, will determine the breadth of its efficacy. Finally, investigating the upstream signalling pathways that lead to the altered BAX/BCL-2 ratio will provide a more complete understanding of the compound's mechanism of action. Also, this study aligns with the UN Sustainable Development Goals (SDG 3: Good Health and Well-Being, SDG 9: Industry, Innovation, and Infrastructure, and SDG 14: Life Below Water) by developing a novel anti-breast cancer agent. In summary, $CuFe_2O_4$ NPs-MK composite synthesized in this work represents a promising nanotherapeutic agent.

Data availability

All data generated or analyzed during this study are included in this published article. The datasets of DNA sequence of the isolated bacterial strain analyzed during the current study are available in the GenBank repository (accession number: PX148123)[https://www.ncbi.nlm.nih.gov/nuccore? term=PX148123](https:/www.ncbi.nlm.nih.gov/nuccore? term=PX148123).

Received: 14 September 2025; Accepted: 27 November 2025
Published online: 06 December 2025

References

1. Dhiwahar, A. T. et al. Improved photocatalytic degradation of Rhodamine B under visible light and magnetic properties using microwave combustion grown Ni doped copper ferrite spinel nanoparticles. *Solid State Sci* **113**, 106542 (2021).
2. Kanithan, S. et al. Enhanced optical, magnetic, and photocatalytic activity of Mg^{2+} substituted $NiFe_2O_4$ spinel nanoparticles. *J Mol. Struct* **1265**,133289 (2022).
3. Wank, I., Amthor, A., Kreitz, S., Häfele, M. & Hess, A. Gene expression patterns decompose fMRI activation in a sub-region-specific manner in mice after nociceptive stimulation. *Neuroimage* **318**, 121425 (2025).
4. Shukla, S., Khan, R. & Daverey, A. Synthesis and characterization of magnetic nanoparticles, and their applications in wastewater treatment: A review. *Environ Technol. Innov* **24**, 101924 (2021).
5. Revathi, R. et al. Facile synthesis of Ni^{2+} Doped $MgFe_2O_4$ spinel nanoparticles: Structural, Optical, Magnetic, and dielectric behavior. *J. Inorg. Organomet. Polym. Mater.* **34**, 374–386 (2024).
6. Mazurenko, J. et al. Synthesis and Characterization of Copper Ferrite Nanoparticles for Efficient Photocatalytic Degradation of Organic Dyes. *J Nanotechnol* (2025). (2025).
7. Feijoo, I. et al. Estimation of crystallite size and lattice strain in nano-sized tic particle-reinforced 6005A aluminium alloy from X-ray diffraction line broadening. *Powder Technol.* **343**, 19–28 (2019).
8. Bhagwat, V. R., Humbe, A. V., More, S. D. & Jadhav, K. M. Sol-gel auto combustion synthesis and characterizations of Cobalt ferrite nanoparticles: different fuels approach. *Mater. Sci. Eng. B* **248**, 114388 (2019).
9. Soufi, A., Hajjaoui, H., Elmoubarki, R., Abdennouri, M. & Barka, N. Sol-gel auto-combustion synthesis of Cu1-xMgxFe_2O_4 nanoparticles and their heterogenous Fenton-like activity towards tartrazine. *Inorg Chem. Commun* **142**, 109717 (2022).
10. Singh, G., Ubhi, M. K., Jeet, K., Singla, C. & Kaur, M. A Review on Impacting Parameters for Photocatalytic Degradation of Organic Effluents by Ferrites and Their Nanocomposites. *Processes* 11, (2023).
11. Balaev, D. A. et al. Interparticle magnetic interactions and the field dependence of the superparamagnetic blocking temperature in a powder system of ultrasmall nickel ferrite particles. *JETP Lett.* **120**, 751–758 (2024).
12. Kefeni, K. K., Mamba, B. B. & Msagati, T. A. M. Application of spinel ferrite nanoparticles in water and wastewater treatment: A review. *Sep. Purif. Technol.* **188**, 399–422 (2017).

13. Carvalho, J. P. F. et al. Potassium Ferrite for Biomedical Applications. *Materials* **16**, *3880 (2023)*.
14. Paswan, S. K. et al. Optimization of structure-property relationships in nickel ferrite nanoparticles annealed at different temperature. *J. Phys. Chem. Solids* **151**, 109928 (2021).
15. Desai, K. R. et al. X-ray diffraction based Williamson–Hall analysis and Rietveld refinement for strain mechanism in Mg–Mn co-substituted $CdFe_2O_4$ nanoparticles. *Physica B Condens. Matter* **614**, 413054 (2021).
16. Anjaneyulu, B., Chauhan, V., Afshari, M. & Chinmay & Enhancing photocatalytic wastewater treatment: investigating the promising applications of nickel ferrite and its novel nanocomposites. *ESPR* **31**, 43453–43475 (2024).
17. Al-Qasmi, N., Al-Gethami, W., Alhashmialameer, D., Ismail, S. H. & Sadek, A. H. Evaluation of Green-Synthesized Cuprospinel nanoparticles as a nanosensor for detection of Low-Concentration Cd(II) ion in the aqueous solutions by the quartz crystal microbalance method. *Materials* **15**, 6240 (2022).
18. Navas, D., Fuentes, S. & Castro-Alvarez, A. & Chavez-Angel, E. Review on Sol-Gel Synthesis of Perovskite and Oxide Nanomaterials. *Gels* **7**, (2021).
19. Hussain, K., Amin, N. & Arshad, M. I. Evaluation of structural, optical, dielectric, electrical, and magnetic properties of Ce^{3+} doped $Cu_{0.5}Cd_{0\cdot25}Co_{0.25}Fe_2$-$xO_4$ spinel nano-ferrites. *Ceram. Int.* **47**, 3401–3410 (2021).
20. SOUFI, A. et al. Spinel ferrites nanoparticles: Synthesis methods and application in heterogeneous Fenton oxidation of organic pollutants – A review. Appl. Surf. Sci. Adv.*s* **6**, (2021).
21. Majid, F. et al. Synthesis and characterization of $NiFe_2O_4$ ferrite: Sol–gel and hydrothermal synthesis routes effect on magnetic, structural and dielectric characteristics. *Mater Chem. Phys* **258**, 123888 (2021).
22. Alamrani, A. & Eldiasty, J. G. Bacterial-extract mediated gold nanoparticles: enhanced uptake, oxidative stress, and cytotoxicity in HepG2 cells with biofilm Inhibition and antibiotic synergy. *Spectrochim Acta Mol. Biomol. Spectrosc.* **345**, 126763 (2026).
23. Metwally, R. A., El-Sersy, N. A., Sikaily, A., El, Sabry, S. A. & Ghozlan, H. A. Vitamin K (Menaquinone) from marine *Kocuria* sp. RAM1: optimization, characterization and potential in vitro biological activities. *Microb Cell Fact.* **24**, 1–19 (2025).
24. Metwally, R. A., El-Sersy, N. A., El Sikaily, A., Sabry, S. A. & Ghozlan, H. A. Optimization and multiple in vitro activity potentials of carotenoids from marine *Kocuria* sp. RAM1. *Sci. Rep.* **12**, 1–19 (2022).
25. Otsuka, T., Mitsuishi, H., Onishi, H. & Yayota, M. Diurnal variation in clock gene expression and progesterone secretion is inhibited under constant light conditions in Japanese black cows. *Reprod. Biol.* **25**, 101056 (2025).
26. Nadeau-Lachance, L., Choquette, T., Khorami, H., Angers, H., Breton, S. & A. & Evaluating the effect of the mitochondrial alternative peptide MTALTND4 on gene expression. *Biochem. Biophys. Rep.* **44**, 102223 (2025).
27. Sheena, T. V., Jyothish, B. & Jacob, J. Preparation, characterization, and in vitro evaluation of the anticancer activity of Ce^{3+} doped $CuFe_2O_4$ spinel nanoparticles in MCF-7 cell lines. *Chem. Phys. Impact*. **8**, 100423 (2024).
28. Yaray, K. et al. $CuFe_2O_4$ decorated with BSA as a potential nanoradioenhancer for enhanced X-ray radiation therapy of brain tumor. *Chem. Pap.* **77**, 7187–7196 (2023).
29. Naderi, E. et al. In vivo and in vitro biocompatibility study of Fe_3O_4@ZnO and Fe_3O_4@SiO_2 as photosensitizer for targeted breast cancer drug delivery. *J. Sci. Islamic Repub. Iran.* **31**, 357–368 (2020).
30. Rotunjanu, S. et al. Newly synthesized $CoFe_2$ – xDy_xO_4 (x = 0; 0.1; 0.2; 0.4) nanoparticles reveal promising anticancer activity against melanoma (A375) and breast cancer (MCF-7) cells int. *J. Mol. Sci. 2023.* **24**, 15733 (2023).
31. Salehiabar, M. et al. Targeted $CuFe_2O_4$ hybrid nanoradiosensitizers for synchronous chemoradiotherapy. *J. Controlled Release*. **353**, 850–863 (2023).
32. Xiong, X. et al. Breast cancer: pathogenesis and treatments. *Sig. Transduct. Target. Ther.* 10, 49 (2025).
33. Hu, C. et al. A Population-Based study of genes previously implicated in breast cancer. *N. Engl. J. Med.* **384**, 440–451 (2021).
34. Alam, M. et al. B cell lymphoma 2: A potential therapeutic target for cancer therapy. *Int. J. Mol. Sci.* **22**, 10442 (2021).
35. Bleicken, S. et al. Bax and Bcl-xL exhibit opposite membrane remodeling activities. *Cell Death & Disease 2016 7:2* 7, e2121–e2121 (2016).
36. Kawiak, A. & Kostecka, A. Regulation of Bcl-2 family proteins in Estrogen Receptor-Positive breast cancer and their implications in endocrine therapy. *Cancers* **14**, 279 (2022).
37. Metwally, R. A., El-Sersy, N. A., El Sikaily, A., Sabry, S. A. & Ghozlan, H. A. Optimization and multiple in vitro activity potentials of carotenoids from marine *Kocuria* sp. RAM1. *Sci. Rep.* **12**, 1–19 (2022).
38. Lane, D. J. 16S/23S rRNA sequencing. In *Nucleic Acid Techniques in Bacterial Systematic* (eds Stackebrandt, E. & Goodfellow, M.) 115–175 (Wiley, 1991).
39. Agudelo-Pérez, S. et al. 16S rDNA sequencing for bacterial identification in preterm infants with suspected Early-Onset neonatal sepsis. *Trop. Med. Infect. Dis.* **9**, 152 (2024).
40. Samal, K. C., Sahoo, J. P., Behera, L. & Dash, T. Understanding the BLAST (Basic Local Alignment Search Tool) Program and a Step-by-step Guide for its Use in Life Science Research. *Bhartiya Krishi Anusandhan Patrika* 36, 55-61 (2021).
41. Kanathala, A. P., Bollempally, P., Kyasarapu, P., Singam, P. & Kethavath, S. N. Genome-wide analysis of rice OsDHSRP gene family and their expression profiles under different abiotic stresses. (2024).
42. Dong, H. et al. Phylogenetic analysis of some species of the Anopheles hyrcanus group (Diptera: Culicidae) in China based on complete mitochondrial genomes. *Genes (Basel)*. **14**, 1453 (2023).
43. Metwally, R. A. et al. Biosynthesis, characterization and optimization of TiO_2 nanoparticles by novel marine halophilic *Halomonas* sp. RAM2: application of natural dye-sensitized solar cells. *Microb. Cell. Fact.* **22**, 1–17 (2023).
44. Alsebaii, N. M., Hegazy, E. Z., Abd El Maksod, I. H., El-Sayed El-Shafay, S. Enhanced photocatalytic activity of titanium-doped copper ferrite for methyl green dye degradation under commercial visible LED light. Ceram. Int. **50**, 45479–45487 (2024).
45. Lee, M. H., Kim, T. E., Jang, H. W., Chun, Y. G. & Kim, B. K. Physical and turbidimetric properties of cholecalciferol- and menaquinone-loaded lipid nanocarriers emulsified with polysorbate 80 and soy lecithin. *Food Chem.* **348**, 129099 (2021).
46. Lone, A. S., Shahnawaz, M., Singh, N., Pervez, S. & Ravindran, K. C. Metabolomic and antioxidant potential analyses of the rhizome and leaves of *Podophyllum hexandrum* royle: A comparative account. *Biocatal. Agric. Biotechnol.* **52**, 102836 (2023).
47. Ughy, B. et al. Reconsidering dogmas about the growth of bacterial populations. *Cells* **12**, 1430 (2023).
48. Keshavarzi, O. et al. Investigating the expression levels of Bax and Bcl-2 genes in peripheral blood lymphocytes of industrial radiation workers in the Asaluyeh region. *J. Biomed. Phys. Eng.* **14**, 275 (2024).
49. Alnaimat, S. M., Abushattal, S. & Dmour, S. M. Draft genome of halophilic *Salinicoccus roseus* H15 isolated from desert rock varnish in Ma'an, Jordan. *Microbiol Resour. Announc* **14**, e00928-24 (2025).
50. Zhou, Z., Tran, P. Q., Cowley, E. S., Trembath-Reichert, E. & Anantharaman, K. Diversity and ecology of microbial sulfur metabolism. *Nat. Rev. Microbiol.* **23**, 122–140 (2025).
51. Vigneron, A. et al. Genomic evidence for sulfur intermediates as new biogeochemical hubs in a model aquatic microbial ecosystem. *Microbiome* **9**, 1–14 (2021).
52. van Vliet, D. M. et al. The bacterial sulfur cycle in expanding dysoxic and euxinic marine waters. *Environ. Microbiol.* **23**, 2834–2857 (2021).
53. Zhang, T. S., Zhang, Y. N., Lu, D. C., Gong, Y. & Du, Z. J. *Carboxylicivirga Marinus* sp. nov., isolated from marine Sediment, and genome insight of the genus *Carboxylicivirga*. *Front. Mar. Sci.* **8**, 731212 (2021).
54. Ramana, C. V. et al. *Salinicoccus halitifaciens* sp. nov., a novel bacterium participating in halite formation. *Antonie Van Leeuwenhoek Int. J. Gen. Mol. Microbiol.* **103**, 885–898 (2013).
55. Chen, Y. G. et al. *Salinicoccus salitudinis* sp. nov., a new moderately halophilic bacterium isolated from a saline soil sample. *Extremophiles* **12**, 197–203 (2008).

56. Hyun, D. W. et al. Genome sequence of the moderately halophilic bacterium *Salinicoccus Carnicancri* type strain CrmT (=DSM 23852T). *Stand. Genomic Sci.* **8**, 255–263 (2013).
57. Nikam, P. N. et al. Synthesis and characterization of $CuFe_2O_4$ spinel ferrite for supercapacitor application. *J. Indian Chem. Soc.* **101**, 101277 (2024).
58. Scherrer, P. Bestimmung der inneren Struktur und der Größe von Kolloidteilchen mittels Röntgenstrahlen. In *Kolloidchemie ein lehrbuch* 387-409. (Berlin, Heidelberg: Springer Berlin Heidelberg,1912).
59. Tarani, E. et al. Calculation of the degree of crystallinity of HDPE/GNPs nanocomposites by using various experimental techniques: a comparative study. *J. Mater. Sci.* **58**, 1621–1639 (2023).
60. Kumar, D. et al. Sustainable high frequency applications of copper ferrite nanoparticles. *Inorg Chem. Commun* **174**, 114018 (2025).
61. Hellwig, P. Infrared spectroscopic markers of Quinones in proteins from the respiratory chain. *Biochim. Et Biophys. Acta (BBA) - Bioenergetics*. **1847**, 126–133 (2015).
62. Maneesha, M., A bioprocess optimization study to enhance the production of Menaquinone-7 using *Bacillus subtilis* MM26. *Microb. Cell. Fact.* **24**, 1–11 (2025).
63. Masunga, N., Mmelesi, O. K., Kefeni, K. K. & Mamba, B. B. Recent advances in copper ferrite nanoparticles and nanocomposites synthesis, magnetic properties and application in water treatment: review. *J. Environ. Chem. Eng.* **7**, 103179 (2019).
64. Dunovska, K., Klapkova, E., Sopko, B., Cepova, J. & Prusa, R. LC-MS/MS quantitative analysis of phylloquinone, menaquinone-4 and menaquinone-7 in the human serum of a healthy population. *PeerJ* e7695 (2019).
65. Xie, F., Pei, S., Lin, X., Tian, Y. & Zhang, G. A rapid and efficient method for the extraction and identification of menaquinones from actinomycetes in wet biomass. *BMC Microbiol.* **21**, 1–10 (2021).
66. Azarkina, N. & Konstantinov, A. A. Stimulation of Menaquinone-Dependent electron transfer in the respiratory chain of *Bacillus subtilis* by membrane energization. *J. Bacteriol.* **184**, 5339–5347 (2002).
67. Ji, P. et al. Potential of copper and copper compounds for anticancer applications. *Pharmaceuticals 2023.* **16**, 234 (2023).
68. Tang, D., Kroemer, G. & Kang, R. Targeting Cuproplasia and Cuproptosis in cancer. *Nat. Rev. Clin. Oncol.* **21**, 370–388 (2024).
69. Tsvetkov, P. et al. Copper induces cell death by targeting lipoylated TCA cycle proteins. *Sci. (1979).* **375**, 1254–1261 (2022).
70. Diao, Y. et al. Dual-responsive magnetic nanozyme Cu-$CuFe_2O_4$ leverages mild magnetic hyperthermia and redox dyshomeostasis to potentiate Cuproptosis. *Colloids Surf. B Biointerfaces*. **257**, 115146 (2026).
71. Li, Z. et al. Recent advances in Nanomaterials-Based Chemo-Photothermal combination therapy for improving cancer treatment. *Front. Bioeng. Biotechnol.* **7**, 488148 (2019).
72. Raisova, M. et al. The Bax/Bcl-2 ratio determines the susceptibility of human melanoma cells to CD95/Fas-Mediated apoptosis. *J. Invest. Dermatol.* **117**, 333–340 (2001).
73. Selim, M. E. & Hendi, A. A. Gold nanoparticles induce apoptosis in MCF-7 human breast cancer cells. *Asian Pac. J. Cancer Prev.* **13**, 1617–1620 (2012).
74. Bojar Doulaby, F., Kavousi, M. & Jamshidian, F. Effect of *Dioscorea* extract on Bax and Bcl-2 gene expression in MCF-7 and HFF cell lines. *EJMHG* **24**, 1–11 (2023).
75. Moradipour, A., Dariushnejad, H., Ahmadizadeh, C. & Lashgarian, H. E. Dietary flavonoid carvacrol triggers the apoptosis of human breast cancer MCF-7 cells via the p53/Bax/Bcl-2 axis. *Med. Oncol.* **40**, 1–7 (2023).
76. Elumalai, K., Srinivasan, S. & Shanmugam, A. Review of the efficacy of nanoparticle-based drug delivery systems for cancer treatment. *Biomed. Technol.* **5**, 109–122 (2024).
77. Sabouri, Z., Sabouri, S., Sabouri, M. & Darroudi, M. Evaluation of sensor Performance, photocatalytic Efficiency, and biological effects of se doped ZnO-Al_2O_3 nanocomposite synthesized with *Nymphaea pygmaea Alba* extract. *Water Air Soil. Pollut.* **236**, 1–13 (2025).
78. Sabouri, Z. et al. Facile green synthesis of Ag-doped ZnO/CaO nanocomposites with *Caccinia Macranthera* seed extract and assessment of their cytotoxicity, antibacterial, and photocatalytic activity. *Bioprocess. Biosyst Eng.* **45**, 1799–1809 (2022).
79. Sabouri, Z., Sammak, S., Sabouri, S., Tabrizi Hafez Moghaddas, S. S. & Darroudi, M. Green synthesis of Ag-Se doped ZnO-Co_3O_4-NiO fivenary nanocomposite using Poly anionic cellulose and evaluation of their anticancer and photocatalyst applications. *Chem. Methodol.* **8**, 164–176 (2024).
80. Sabouri, Z. et al. Plant-mediated synthesis of Ag and Se dual-doped ZnO-CaO-CuO nanocomposite using *Nymphaea alba L.* extract: assessment of their photocatalytic and biological properties. *Biomass Convers. Biorefin.* **14**, 32121–32131 (2024).
81. Yu, S., Zhang, H., Zhang, S., Zhong, M. & Fan, H. Ferrite Nanoparticles-Based reactive oxygen Species-Mediated cancer therapy. *Front. Chem.* **9**, 651053 (2021).
82. Srikanth, K. & Nutalapati, V. Copper ferrite nanoparticles induced cytotoxicity and oxidative stress in channel catfish ovary cells. *Chemosphere* **287**, 132166 (2022).
83. Mushtaq, S. et al. Biocompatibility and cytotoxicity in vitro of surface-functionalized drug-loaded spinel ferrite nanoparticles. *Beilstein J. Nanotechnol.* **12**, 1339–1364 (2021).

Acknowledgements

The authors are extremely grateful to King Abdul-Aziz University, Jeddah, Saudi Arabia and the Faculty of Education, Physics and Chemistry Department, Matrouh University, Mersa Matrouh, Egypt, for providing all the facilities to complete this work.

Author contributions

R.M.F. and M.S.A. performed the experimental part, prepared all figures, interpreted the data, carried out the analysis and wrote the main manuscript text. M.S.A. helped in the identification and extraction of MK and data interpretation. All authors read and approved the final manuscript.

Declarations

Competing interests

The authors declare no competing interests.

Additional information

Correspondence and requests for materials should be addressed to R.M.F. or M.S.A.